Research Article Vol. 33, No. 6 / 24 Mar 2025 / Optics Express 14035

Optics EXPRESS

Optimized photon routing with a silicon 3 × 3 waveguide coupler device

SALAMAT ALI,* RICCARDO FRANCHI, STEFANO BIASI, BÜLENT ASLAN, AND LORENZO PAVESI

Nanoscience Laboratory, Department of Physics, University of Trento, 38123 Povo, Italy
**salamat.ali@unitn.it*

Abstract: In integrated photonics, the precise control and routing of light signals is crucial. Conventionally, light routing in photonic devices is achieved using multi-mode interferometers and microresonators. An alternative approach is to use $n \times n$ waveguide couplers. In this study, we explore the use of such devices both theoretically and experimentally in the realization of a versatile 3×3 coupler on the silicon photonics platform. We demonstrate that this device can effectively route signals in multiple ways: crossing signals between the external waveguides for a specific coupling, or distributing signals evenly across the three output waveguides, as well as functioning as a versatile switch for other arbitrary output combinations. By fitting the experimental results with a theoretical model, we extracted its characteristic parameters, highlighting both the model's behavior and the impact of non-idealities. Our work lays the foundation for the design of an efficient and tunable 3×3 waveguide coupler device.

1. Introduction

Coupled waveguide arrays have been widely used in photonics to study various phenomena ranging from non-Hermitian physics [1,2], to quantum systems [3,4] and to artificial neural networks [5,6]. To study these effects, precise control over light and its routing is pivotal. Conventionally, light routing is achieved using multimode interferometer (MMI) [7], directional couplers [8], coupled ring resonators [9], and also adiabatic passage to improve the robustness of simple directional couplers [10–12]. For a multiport device, either cascading of simple 2 couplers or direct coupling n waveguides are used [5,13–16].

Despite growing interest in $n \times n$ devices for photonic integrated circuits (PICs), comprehensive studies that compare theoretical predictions with experimental results are still lacking. To provide a basis for future development, we present here the analysis of the experimental response of a 3×3 coupler showing the trend of the characteristic parameters obtained through a fitting process. Several other studies have implemented 3×3 couplers on different material platforms and for other applications. For instance, Ref. [17] explored 3×3 couplers on $LiNbO_3$ but without thermal tuning, while Ref. [18] investigated 3×3 MMI couplers in InP. Additionally, Ref. [19] focuses on silicon-on-insulator SOI wavelength-independent directional couplers and Ref. [20] on 3×3 coupler-based microring resonators for sensing applications.

A 3×3 device can be realized by the evanescent field coupling of the optical modes in a system of three straight waveguides. Here, the coupling can be controlled by design parameters or by varying the waveguide refractive index of the waveguide by using microheaters positioned above the waveguides. We have demonstrated, both theoretically and experimentally, that in 3×3 couplers, light can be routed from each input port to a combination of output ports. To accomplish this, we have designed and tested various 3×3 couplers based on silicon waveguides, see Fig. 1. We characterized the experimental results using coupled mode theory, demonstrating that the device can cross-route the signal between the external waveguides while leaving the central waveguide signal unchanged or achieving a balanced output across all three output ports.

#551702 https://doi.org/10.1364/OE.551702
Journal © 2025 Received 10 Dec 2024; revised 4 Feb 2025; accepted 13 Feb 2025; published 19 Mar 2025

Optics EXPRESS

To further manage the splitting ratio of light, we utilized an active micro-heater on top of the central waveguide, controlled by current, resulting in a change in the propagation and coupling parameters. This allows both crossing and splitting functionalities. We characterized our structures by extracting characteristic parameters from experimental data, collected by varying both the wavelength and the electrical power applied to the micro-heater.

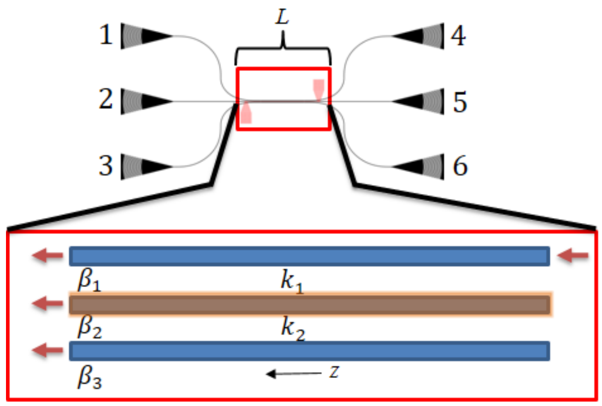

Fig. 1. The 3×3 coupler device. The three grating couplers on the right (triangles numbered from 4 to 6) represent the input ports, while the three on the left (triangles numbered from 1 to 3) represent the output ports. These ports are connected by a 3×3 coupler of length L. The light orange pads indicate the electrical contacts where the current is applied. The red rectangle encircles the three equally spaced and equal-length coupled waveguides, with a micro-heater (transparent brown layer) placed on top of the central waveguide for thermal tuning.

2. Theory and design

We examine a configuration of three coupled waveguides, which are equally spaced and of equal lengths, as shown in Fig. 1. We employ coupled mode theory (CMT), a method highly effective for characterizing the behavior of weakly coupled three-waveguide directional couplers with a constant coupling coefficient [13,21]. Additionally, the theory assumes that the external waveguides do not interact with each other due to the exponential decay of their coupling fields.

We aim to establish a general method, as described in [21], to relate the electric field at the waveguides entry at $z = 0$ to the electric field at their exit, at $z = L$, where z represents the propagation direction of the wave and L is the length of the coupling section of the waveguides in the structure, as shown in Fig. 1. To achieve this, we construct a transformation matrix, T, to show the field propagation in three coupled waveguides in the following way:

$$\mathbf{E}(z = L) = T\mathbf{E}(z = 0)\,. \tag{1}$$

Due to the lateral separation between the waveguides, the segments of each waveguide from the grating couplers (numbered pads in Fig. 1) to the coupling section are assumed to be negligible in influencing light propagation. To obtain T, we begin by defining the coupling matrix M, which encapsulates the interactions within the system using the following set of differential equations [22–24],

$$-i\frac{d\mathbf{E}(z)}{dz} = M\mathbf{E}(z) \tag{2}$$

Here, $\mathbf{E}(z)$ is a vector associated with the electric field for each waveguide as a function of propagation distance z, i.e., $\mathbf{E}(z) = [E_1(z); E_2(z); E_3(z)]$. M is the coupling matrix governing the

Optics EXPRESS

interactions in the coupled system [24],

$$M = \begin{bmatrix} \beta_1 & k_1 & 0 \\ k_1 & \beta_2 & k_2 \\ 0 & k_2 & \beta_3 \end{bmatrix}$$

where β_n are the propagation constants for each waveguide (from top to bottom: $n = 1, 2, 3$), k_1 is the coupling coefficient between the top and middle waveguides, and k_2 is the coupling coefficient between the middle and bottom waveguides. The couplings between the waveguides are assumed to be Hermitian, and the coefficients are considered to be real and positive.

We then compute the eigenvalues λ_i and the eigenvectors v_i of the M matrix. These calculated eigenvalues λ_i and associated eigenvectors v_i of matrix M form the foundational components for the transformation matrix. By using the eigenvectors, we construct the modal matrix M_g which is the transpose of the matrix formed by the eigenvectors.

The evolution matrix U is calculated using the expression:

$$U = e^{-iDz}, \tag{3}$$

where D is the diagonal matrix of the eigenvalues. The exponential term e^{-iDz} represents the evolution of the three supermodes of the system under the influence of the eigenvalues λ_i over the spatial coordinate z.

Finally, the transformation matrix T takes the following form:

$$T = M_g U M_g^{-1}. \tag{4}$$

Through the construction of this transformation matrix T, we establish a linear relation that maps the field from the initial position $z = 0$ to the final position $z = L$, thereby providing a systematic approach to calculate the outputs of the fields.

In general, the knowledge of T allows relating any input to any output. In the specific example we are showing in Fig. 1, matrix T has a simplified expression. In fact, given the symmetry of the external waveguides, we can assume $\beta_1 = \beta_3$. In addition, we define $\Delta\beta = \beta_2 - \beta_1 = \beta_2 - \beta_3$. Additionally, we account for fabrication errors in the structure, making $\Delta\beta$ an intrinsic property of our static device. Using these definitions, the coupling matrix takes the following form:

$$M_1 = \begin{bmatrix} 0 & k_1 & 0 \\ k_1 & \Delta\beta & k_2 \\ 0 & k_2 & 0 \end{bmatrix} \tag{5}$$

It is worth noting that changing the sign of $\Delta\beta$ does not affect the output intensities of the structure. Note that the microheater placed on top of the central waveguide (Fig. 1) allows tuning β_2, i.e., $\Delta\beta$.

We then compute the transformation matrix T_1 for Matrix M_1 by following the procedure outlined in Eqs. (1) to (4). Consequently, T_1 takes the following form:

$$T_1 = \begin{bmatrix} a_{41} & a_{51} & a_{61} \\ a_{42} & a_{52} & a_{62} \\ a_{43} & a_{53} & a_{63} \end{bmatrix}, \tag{6}$$

where a_{ij} are the complex amplitude coefficients with the first and second index referring to the input and output ports, respectively. The explicit form of T_1 is reported in the appendix.

Optics EXPRESS

Assuming that there is no loss (see Appendix for more about losses) and the incident light is distributed among the waveguides, the following conditions hold true for each column of matrix T_1:

$$|a_{i1}|^2 + |a_{i2}|^2 + |a_{i3}|^2 = 1,$$

where $i = 4, 5, 6$ refer to each input port. This is the equation of a sphere in a 3-dimensional space defined by a_{i1}, a_{i2}, and a_{i3}. Thus, we have many solutions for the values of a_{i1}, a_{i2}, and a_{i3} that represent the points on the surface of this sphere. The specific solutions or points on the sphere depend on how a_{i1}, a_{i2}, and a_{i3} are functionally related to k_1, k_2, and $\Delta\beta$. These parameters are real in our model.

Now, let us analyze a simple symmetric scenario when light is injected in port 4. We set $\Delta\beta = 0$ and $k_1 = k_2 = k$ (three perfectly equal waveguides with the same gap between adjacent waveguides). If we want to achieve a complete transfer of the input signal from port 4 to port 3, we have to tune the 3×3 coupler parameters such that:

$$|a_{41}(L)|^2 = |a_{42}(L)|^2 = 0, \quad |a_{43}(L)|^2 = 1\,. \tag{7}$$

This condition is met for discrete values of the coupling coefficient k given by:

$$k_m := (2m-1)\,\frac{\pi}{\sqrt{2}L}, \quad \text{where } m = 1, 2, 3, \ldots \tag{8}$$

as it is clear from Eq. (18) reported in the appendix.

Figure 2 illustrates the outputs for ports 1, 2, and 3 when the input signal is injected into ports 4 (gray color scale) or 5 (cool scale) or 6 (autumn scale) as a function of the coupling $k_2 = k_1 = k$ value ranging from 0 to $\frac{\pi}{\sqrt{2}L}$ at $z = L = 60\,\mu$m. We can represent the outputs as a point laying on a sphere, where the axis of the sphere are nothing else than the field mode intensities in each output waveguides. Consequently, the points representing different combinations of input to outputs, normalized and summed to unity following the energy conservation, form a surface on a unit sphere. Notice that, when the coupling between the waveguides is equal to zero ($k = 0$, darker hues), the light remains in the same waveguide. Consequently, $|a_{41}| = 1$, $|a_{52}| = 1$ and $|a_{63}| = 1$ (left, top and right corners of the eighth of the sphere).

In Fig. 2(c), it is observed that when the system is excited from port 4, with increasing k, the light passes from the top waveguide to the middle waveguide, fully reaching the bottom one at $k = \frac{\pi}{\sqrt{2}L}$ (from left to top corners of the sphere in Fig. 2(a)). Due to the symmetry of the structure, the line corresponding to the excitation from port 6 is similar to the one corresponding to the excitation from port 4, and so the output field starts from the top corner and reaches the left corner of the sphere, see autumn color scale line in Fig. 2. On the other hand, as shown in Fig. 2(d), when light is fed from port 5 (middle waveguide), increasing k, the electromagnetic wave passes symmetrically from the middle waveguide to the external (top and bottom) waveguides reaching the combination $(|a_{i1}|^2, |a_{i2}|^2, |a_{i3}|^2) = (0.5, 0, 0.5)$ at $k = \frac{\pi}{2\sqrt{2}L}$. As can be seen from the cool color scale curve in Fig. 2, after this point the light gradually returns to the central waveguide, exiting from port 2 for $k = \frac{\pi}{\sqrt{2}L}$. Note also that in this figure the lines corresponding to the excitation from port 6 and the second half of the excitation from port 5 have been plotted in Fig. 2(b) to give a clearer picture.

It is worth noting that Fig. 2 shows a very specific case, where the structure is symmetric and $\Delta\beta = 0$ (three equal waveguides). However, the solutions presented here are general and can be used in cases where the structure is asymmetric and the waveguides are different.

Optics EXPRESS

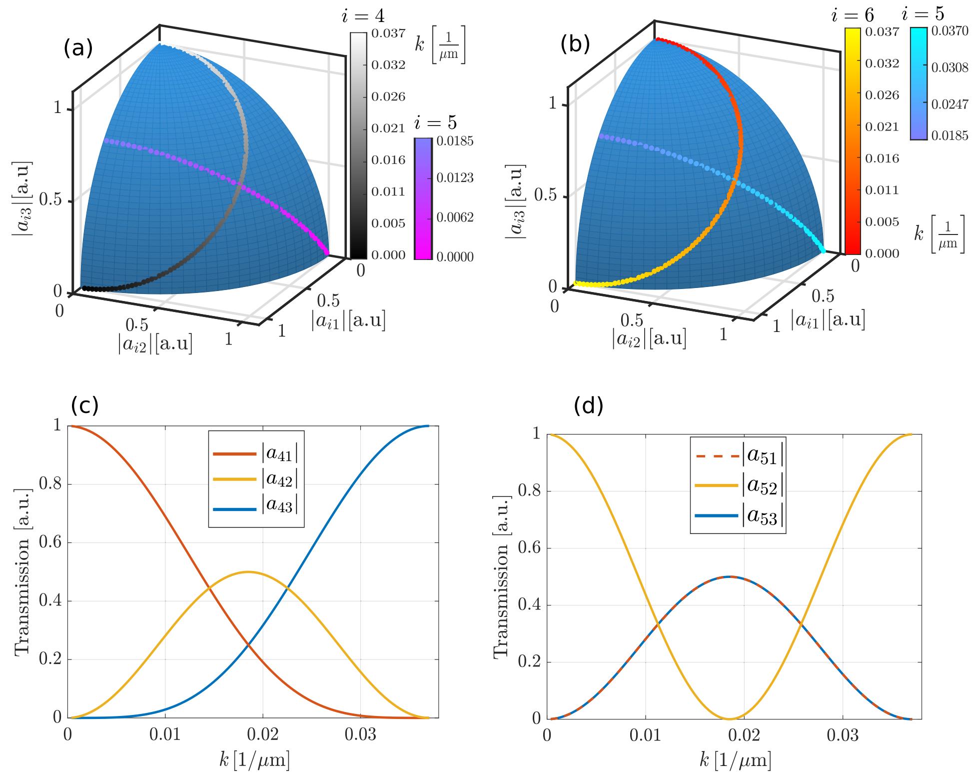

Fig. 2. Theory. Three dimensional visualization of the output combinations of the structure for a single excitation from ports $i = 4, 5, 6$ as a function of the coupling parameter $k = k_1 = k_2$, ranging from 0 to $k = \frac{\pi}{\sqrt{2}L}$, where $L = 60\,\mu$m. (a) shows the outputs for excitation from port $i = 4$ (gray scale color), varying from $k = 0$ to $k = \frac{\pi}{\sqrt{2}L}$, along with the excitation from port $i = 5$ (violet scale color) for k ranging from 0 to $k = \frac{\pi}{2\sqrt{2}L}$. (b) shows the output for excitation from port $i = 6$ (cyan scale color), varying from $k = 0$ to $k = \frac{\pi}{\sqrt{2}L}$, along with the excitation from port $i = 5$ (violet scale color) for k ranging from $k = \frac{\pi}{2\sqrt{2}L}$ to $k = \frac{\pi}{\sqrt{2}L}$. (c) and (d) show the transmission outputs for excitation from ports 4 and 5, respectively. Note: the output combinations for excitation from port 6 can be inferred from (c) by replacing $|a_{43}|$ with $|a_{61}|$, $|a_{42}|$ with $|a_{62}|$ and $|a_{41}|$ with $|a_{63}|$.

3. Experimental measurements

3.1. Experimental samples and setup

The 3×3 waveguide coupler device is based on 450 nm $\times$ 220 nm silicon waveguides embedded in a silica cladding. The input and output ports are provided by grating couplers. These allow coupling only the Transverse Electric (TE) mode. The waveguide cross section is designed to ensure single-mode operation. The device was fabricated in a run at the IMEC/Europractice facility as part of a multi-project wafer program. The coupling region of the device has waveguide lengths of 60 µm and an inter-waveguide gap of 0.25 µm. Note that the gap and length of the coupling region rule the energy exchange that occurs via the evanescent field. In addition, the device is tunable via current injection through a micro-heater positioned above the central waveguide. Alternatively, one can use a p-i-n junction across the waveguide to achieve a faster tuning. The metal used for the microheater is Titanium Nitride (TiN), which operates as a 345 Ω resistor. The micro-heater is operated with an injected electrical current from 0 mA to 16 mA.

We explore the transmission through the output ports under two distinct conditions: (1) in the absence of electrical current flow through the microheater, where the device is passive, and (2) with an injected electrical current, where the device is active. Measurements are made using a typical optical characterization setup. A fiber-coupled tunable continuous-wave laser is used as the source. It operates at 3 mW with a tunable wavelength range from 1490 nm to 1640 nm. The light polarization is tuned by a fiber polarization controller and the signal is coupled to the grating coupler by a stripped fiber mounted on an alignment stage. The output signal from the structure is collected by another stripped fiber and sent to a detector. A write-board (Measurement Computing USB-3106) with an amplification stage controls the current applied to the micro-heater. The optical chip is placed on a thermostat holder whose temperature is controlled by a proportional-integral-derivative controller connected to a Peltier cell and a 10kΩ thermistor.

3.2. Results and discussion

Figure 3 shows the experimental results and fitting parameters obtained using the theoretical model for an input signal at ports 4, 5, and 6. Figures 3(a)–(c) show the output transmission at the different output ports as a function of input wavelength and their fit when there is no electrical current applied to the micro-heater. In our fitting procedures, all nine experimental output signals corresponding to each input-output combination were used simultaneously to increase the overall confidence in the fitting. This combined fitting was performed with the parameters allowed to vary freely. For the device with no current applied, the sum of the normalized Squared Residuals (SSR) with respect to the model was found to be $SSR = 1.1 \times 10^{-5}$, while when current is applied, $SSR = 5.3 \times 10^{-3}$. During the fitting, the experimental data were normalized to the sum of the transmissions at the output ports for each input. Therefore, an SSR much smaller than 1 means a very good agreement between the model and the measured data. Since the designed structure is composed of three equal waveguides with the same gap, we simplify the general equation using the assumption $\Delta\beta = \beta_2 - \beta_1 = \beta_2 - \beta_3$. In addition, we allow for $k_1 \neq k_2$ to account for fabrication errors. The extracted parameters are illustrated in Fig. 3(d). We observe that the coupling coefficients k_1 and k_2, although slightly different, increase with increasing wavelengths.

This is particularly noticeable at longer wavelengths. This phenomenon can be attributed to the enhanced mode spreading within the waveguides. Since the mode confinement in each waveguide decreases for longer wavelengths, there is a greater extent of mode overlap across the waveguides, facilitating stronger coupling.

Despite the structures being designed to exhibit identical coupling between the waveguides, we observed a slight difference between the extracted k_1 and k_2. This suggests the presence of imperfections arising from the fabrication processes and results in a nonzero $\Delta\beta$ term. Note that $\Delta\beta \simeq 0.05$ $1/\mu$m is easily explained by fabrication errors. In fact, it corresponds to a change in waveguide width of about 7 nm (see Fig. 6 in the Appendix). This value is in agreement with the value of the standard deviation of the waveguide width declared by IMEC. Additionally, the observed decrease in $\Delta\beta$ as a function of increasing wavelength is coherent with the relationship $\Delta\beta = \frac{2\pi}{\lambda}(n_{\mathrm{eff},2} - n_{\mathrm{eff},1})$, where $n_{\mathrm{eff},i}$ is the effective refractive index of the waveguide number i and λ is the wavelength. As shown in Figs. 3(a)–(d), changing the wavelength changes the parameters of the structure. This gives rise to a variation of the ratio between the intensities at the output ports.

Let us now focus on two specific situations highlighted by the colored boxes in Fig. 3. The first case is represented by the gray box at $\lambda = 1560$ nm and corresponds to $\Delta\beta \simeq 0.029 \pm 1.56 \times 10^{-5}$ $1/\mu$m, $k_1 = 0.022 \pm 5.25 \times 10^{-6}$ $1/\mu$m, and $k_2 = 0.021 \pm 5.67 \times 10^{-6}$ $1/\mu$m. By injecting light into any of the input ports (4, 5, 6), the intensities at the output ports (1, 2, 3) are almost

Optics EXPRESS

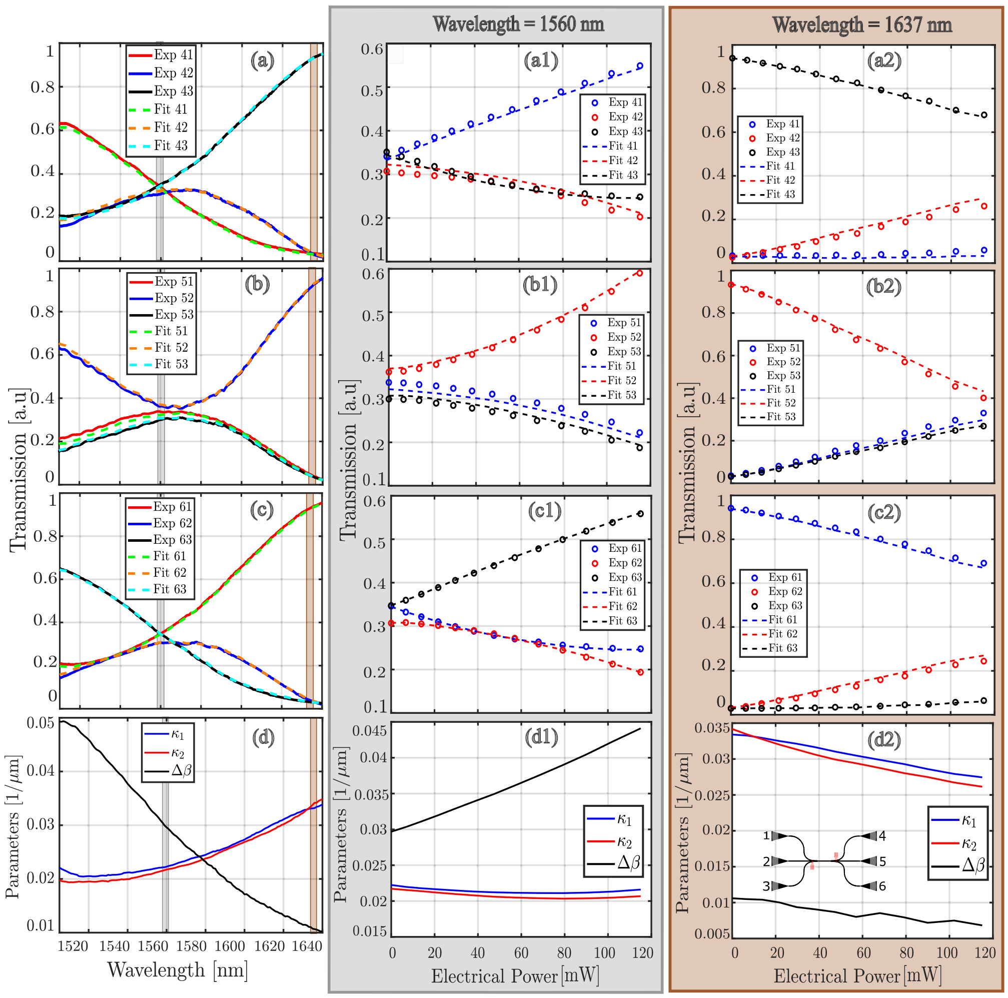

Fig. 3. Experimental results and extracted parameters. (a) to (c) show the measured transmission spectra (solid lines) and fit (dashed lines) for single excitation from ports 4, 5, and 6, respectively. (d) provides the values of k_1, k_2, and $\Delta\beta$ extracted from the fit for a passive device (no electrical power applied). (a1)–(c1) [(a2)–(c2)] depict the measured (empty circles) and fit (dashed lines) output intensities at λ = 1560 nm [λ = 1637 nm], as indicated with a grey [brown] bar in the top panels, as a function of the power delivered to the micro-heater. (d1) and (d2) display variations in k_1, k_2, and $\Delta\beta$ extracted from the fit as a function of the power delivered to the micro-heater. The numbering in the legend: the first number refers to the input port and the second to the output port.

equal, indicating that the optical power is equally split among the output channels, as shown in Figs. 3(a)–(c). This equal distribution of optical power demonstrates the symmetric behavior of the system at this specific wavelength, where each output port receives approximately one-third of the input power, ensuring balanced operation.

In contrast, for the second case at λ = 1637 nm, the power distribution exhibits selective routing behavior. When light is injected into port 4, the signal is routed to port 3, as shown in Fig. 3(a), while the intensities at ports 1 and 2 approach zero . Similarly, injecting light into port 5 routes the signal to port 2, with the output at the ports 1 and 3 reduced to nearly zero, as depicted in Fig. 3(b). When light is injected into port 6, the signal is directed to port 1, with

Optics EXPRESS

output at ports 2 and 3 simultaneously approaching zero, as illustrated in Fig. 3(c). This selective routing indicates that at λ = 1637 nm, the system preferentially directs power to specific output ports based on the input port used, enabling cross-routing between the external waveguides.

Starting from these initial states, as we increase the electrical power delivered to the micro-heater, the parameters of the system are altered, leading to a redistribution of the output field ratios, as illustrated in Figs. 3(a1)–(d1) and (a2)–(d2). Figure 3(a1) demonstrates that at an electrical power of 115.08 mW, the intensity at port 1 reaches 55%, while port 2 settles at 20% and port 3 decreases to 25% . When light is injected from port 5, as shown in Fig. 3(b1) with an electrical power of 115.08 mW, port 2 now has the output value of 60%, while ports 1 and 3 are reduced to values around 20%. Similarly, in Fig. 3(c1), we observe behavior akin to that in Fig. 3(a1): when light is initially coupled to one of the external waveguides, more light remains in the same waveguide, while less light couples to the others as the electrical power is increased. This is due to the design symmetry. Note that the experimental points in the graphs are well-fitted by the theoretical model (dashed lines). The extracted parameters from the fit are shown in Fig. 3(d1). Notice that $\Delta\beta$ increases to 0.045 1/μm from 0.030 1/μm with the application of approximately 115 mW of electrical power. Since the micro-heater is positioned over the central waveguide, this is expected because the increase of $\Delta\beta$ means a faster increase of the effective refractive index of the central waveguide with respect to that of the external waveguides. Additionally, at 1560 nm, the coupling coefficients k_1 and k_2 remain almost constant as a function of the electrical power. This stability is attributed to the high confinement of the optical mode within the waveguide at this particular wavelength, which remains relatively stable despite the temperature changes induced by the micro-heater. Figures 3(a2)–(d2) show the results at λ = 1637 nm. At this wavelength, when the light enters from port 4 exits almost entirely through port 3, the light from port 5 exits through port 2, and the light from port 6 exits through port 1 (see Figs. 3(a)–(c)). In essence, light traverses (crosses) between the external waveguides while remaining confined within the middle waveguide. However, when the micro-heater is activated, the light distribution at the output ports changes for the same input. As a result, some of the light that previously exited through one of the external waveguides (port 1 or port 3) is now routed through the middle waveguide and exits at port 2. Additionally, only a very small percentage of the input light exits from the same waveguide (i.e., output port 1 (3) for input port 4 (6)) as illustrated in Figs. 3(a2) and (c2). In fact, for these two cases, the observed distribution of light at the output ports is 70% , 25% and 5% at 115 mW of electrical power. On the other hand, when the light is injected into the middle waveguide (port 5), some of the light that previously exited through the same waveguide (port 2) is equally routed through the external waveguides and exits at port 1 and port 3 (see Fig. 3(b2)). The observed distribution of light at the output ports is 40%, 30% and 30% at 115 mW of electrical power.

Figure 3(d2) shows the parameters extrapolated from the fit for λ = 1637 nm. Here we see that at longer wavelength, both k_1 and k_2 values exhibit a decrease as the electrical power increases. This trend is not observed at λ = 1560 nm (see Fig. 3(d1)). This can be explained by the fact that, at longer wavelengths, the light confinement inside the waveguide is lower and consequently the coupling coefficients are more sensitive to the variation of the effective refractive index of the waveguide. Figure 3(d1) shows an increasing $\Delta\beta$ as a function of the injected electrical power, while Fig. 3(d2) shows a decreasing behavior. The behavior of $\Delta\beta$ in Fig. 3(d1) could be explained by the fact that β decreases as a function of wavelength (making the $\Delta\beta$ variation less pronounced), and by the fact that the optical mode of the waveguide is less confined and therefore less affected by local temperature variations. On the contrary, the slight decrease of $\Delta\beta$ as a function of power in Fig. 3(d2) cannot be explained in this way. This behavior may be due to either an imperfect noisy fit or to the fact that coupled mode theory is valid for small couplings and well-confined waveguide modes. In the present case, where the coupling is high and the

Optics EXPRESS

confinement of the light is low, the parameters obtained are not directly related to those of the ideal case.

In Fig. 4(a), the output intensities are shown for signal input at ports 4, 5, and 6. Output intensities are normalized and mapped onto the surface of a sphere as a function of wavelengths and injected electrical power. The various colors, as shown in the color bars, represent an increase in wavelength, while the size of the dots, from smaller to bigger, indicates the increase of the injected electrical power. The distribution of points on the sphere surface illustrates the range of output combinations achievable by the system.

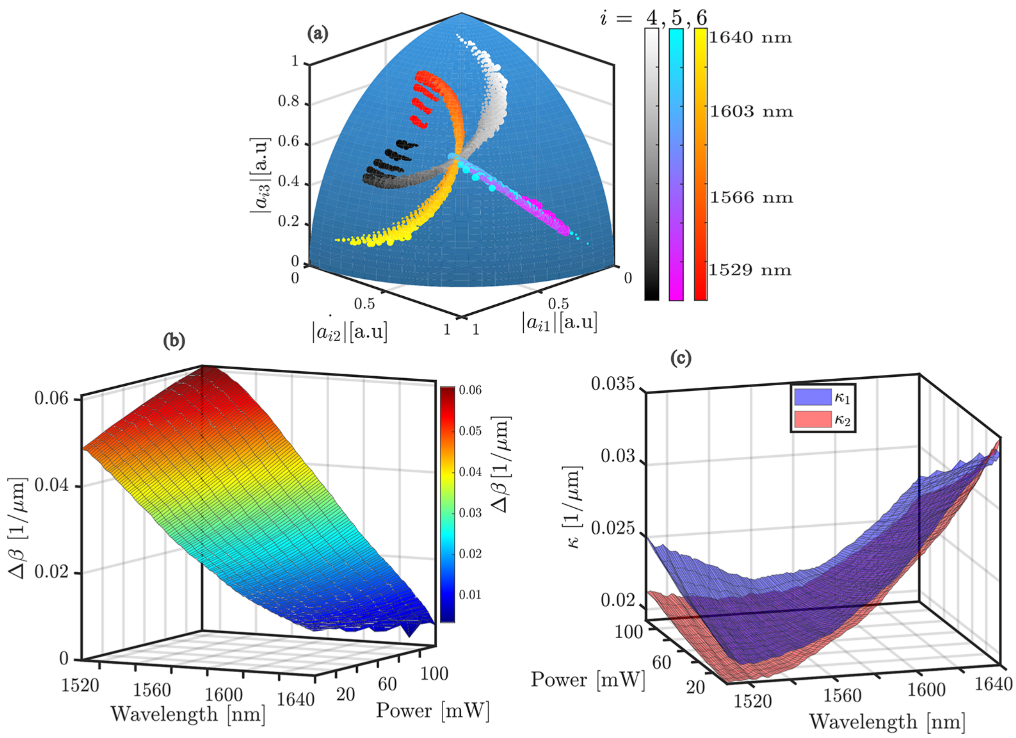

Fig. 4. Representations on a sphere and extracted parameters. (a) displays the experimental outputs for combinations 4, 5, and 6, mapped onto the surface of a sphere as a function of increasing wavelength values and injected electrical power from smaller to larger dots. (b) and (c) present the extracted $\Delta\beta$ values and coupling coefficients, respectively, derived from simultaneous fits of the output signals.

From a fit of the experimental data, the characteristic device parameters are extracted. Figure 4(b) shows a wavelength dependent $\Delta\beta$ value increase with rising injected electrical power. Furthermore, Fig. 4(c) reveals that at injected electrical power lower than 60 mW, as the wavelength increases, the coupling constant values — though slightly different — are consistently increasing. However, at higher injected power levels, not only the difference between k_1 and k_2 widens for lower wavelengths, but also k_1 and k_2 decrease before rising again with further increases in wavelength. This unexpected increase of the coupling coefficients at short wavelengths as the injected power increases could be due to the simplified model used to fit the data. In fact, we have assumed that $\beta_1 = \beta_3$ and that the micro-heater is symmetrically positioned on top of the central waveguide. However, as can be observed from Figs. 3(d) and 4(c), at lower wavelength we detect an asymmetry in the structure. This asymmetry is more relevant at shorter wavelengths because the optical mode is more confined and thus more sensitive to

Optics EXPRESS

local perturbations. For these reasons, at shorter wavelengths, the fabrication errors, e.g., in the symmetry of the waveguides and position of the micro-heater) and the simplified model make the parameters obtained from the fit less physically meaningful.

4. Conclusion

We investigated, both theoretically and experimentally, a 3×3 waveguide coupler device capable of routing light signal between three input ports (4, 5, 6) and three output ports (1, 2, 3) in various combinations. For specific coupling condition or wavelength, we demonstrated that the device can cross the signals between the external waveguides, i.e., from input port 4 to output port 3 and from input port 6 to output port 1, while pass the signal in the central waveguide. In addition, the device can realize other input-output combinations, such as a balanced split of the input to all three output ports (1, 2, 3). To achieve this, a careful selection of the coupling values, or of the wavelength, is needed. When a micro-heater atop the central waveguide is activated, it induces a variation of the propagation constant of the central waveguide and modulates the coupling coefficients between the waveguides. This variation yields an effective modal index mismatch between the central and external waveguides, thereby redirecting the signals from one output port to another. Consequently, the device enables output signal re-routing. Our model of the device allows extracting the characteristic device parameters (coupling coefficients and propagation constants), which vary with injected electrical power and signal wavelength, from the experimental measurements. Consequently, this study provides a comprehensive parameter space for the various routing combination achievable within the 3×3 coupler device. As a final note, similar functionalities can be achieved using Multi-Mode Interferometers and Mach-Zehnder Interferometers. However, the 3×3 coupler device has a small footprint, a simple design and an excellent tunability between input and output ports. These features make it particularly suitable for easy integration into more complex photonic circuits such as photonic neural networks or quantum interference devices. Finally, a potential extension of this study to quantum photonics could be relevant. In fact, three coupled waveguides can form a three-level system where a single photon exists as a superposition of path-encoded qutrit states [25].

Appendix

We report here the analytical functions derived from the matrix M_1 used in Eq. (5). These functions are the elements of the transformation matrix T_1 mentioned in Eq. (6):

Let us define $\alpha = \sqrt{\Delta\beta^2 + 4(k_1^2 + k_2^2)}$ for simplification.

$$a_{41} = \frac{1}{2(k_1^2 + k_2^2)\alpha}\left[e^{-\frac{1}{2}i(\Delta\beta+\alpha)z}\left(\Delta\beta k_1^2(-1 + e^{i\alpha z}) + (k_1^2 + e^{i\alpha z}k_1^2 + 2e^{\frac{1}{2}i\alpha z}k_2^2)\alpha\right)\right], \tag{9}$$

$$a_{42} = -\frac{2ie^{-\frac{1}{2}i\Delta\beta z}k_1 \sin\left(\frac{1}{2}\alpha z\right)}{\alpha}, \tag{10}$$

$$a_{43} = \frac{1}{2(k_1^2 + k_2^2)\alpha}\left[e^{-\frac{1}{2}i(\Delta\beta+\alpha)z}k_1 k_2\left(\Delta\beta(-1 + e^{i\alpha z}) + (1 - 2e^{\frac{1}{2}i(\Delta\beta+\alpha)z} + e^{i\alpha z})\alpha\right)\right], \tag{11}$$

$$a_{51} = -\frac{2ie^{-\frac{1}{2}i\Delta\beta z}k_1 \sin\left(\frac{1}{2}\alpha z\right)}{\alpha}, \tag{12}$$

$$a_{52} = e^{-\frac{1}{2}i\Delta\beta z}\left(\cos\left(\frac{1}{2}\alpha z\right) - \frac{i\Delta\beta \sin\left(\frac{1}{2}\alpha z\right)}{\alpha}\right), \tag{13}$$

Optics EXPRESS

$$a_{53} = -\frac{2ie^{-\frac{1}{2}i\Delta\beta z}k_2 \sin\left(\frac{1}{2}\alpha z\right)}{\alpha}, \tag{14}$$

$$a_{61} = \frac{1}{2(k_1^2+k_2^2)\alpha}\left[e^{-\frac{1}{2}i(\Delta\beta+\alpha)z}k_1k_2\left(\Delta\beta(-1+e^{i\alpha z}) + (1+e^{i\alpha z} - 2e^{-\frac{1}{2}i(\Delta\beta+\alpha)z})\alpha\right)\right], \tag{15}$$

$$a_{62} = -\frac{2ie^{-\frac{1}{2}i\Delta\beta z}k_2 \sin\left(\frac{1}{2}\alpha z\right)}{\alpha}, \tag{16}$$

$$a_{63} = \frac{1}{2(k_1^2+k_2^2)\alpha}\left[e^{-\frac{1}{2}i(\Delta\beta+\alpha)z}\left(\Delta\beta k_2^2(-1+e^{i\alpha z}) + (k_2^2 + e^{i\alpha z}k_2^2 + 2k_2^2k_1^2e^{\frac{1}{2}i(\Delta\beta+\alpha)z})\alpha\right)\right]. \tag{17}$$

The transformation matrix T takes a simple form when the coupling is symmetric ($k_1 = k_2 = k$) and detuning is zero ($\Delta\beta = 0$):

$$T = \begin{pmatrix} \cos^2\left(\frac{kz}{\sqrt{2}}\right) & -\frac{i\sin\left(\sqrt{2}kz\right)}{\sqrt{2}} & -\sin^2\left(\frac{kz}{\sqrt{2}}\right) \\ -\frac{i\sin\left(\sqrt{2}kz\right)}{\sqrt{2}} & \cos\left(\sqrt{2}kz\right) & -\frac{i\sin\left(\sqrt{2}kz\right)}{\sqrt{2}} \\ -\sin^2\left(\frac{kz}{\sqrt{2}}\right) & -\frac{i\sin\left(\sqrt{2}kz\right)}{\sqrt{2}} & \cos^2\left(\frac{kz}{\sqrt{2}}\right) \end{pmatrix} \tag{18}$$

Optical power loss in 3×3 coupler with microheater and propagation constant simulation

To evaluate the impact of power loss as a result of microheater heating when electrical power is applied, we measured the sums of the transmitted signals from the three outputs (41+42+43, 51+52+53, and 61+62+63) and normalized them to their values at zero applied electrical power. Figure 5(a) illustrates how these sums evolve for 1560 nm, when changing the applied electrical power. As depicted, random variations of about 3.3 % are observed. These variations are attributed to several factors: (i) mechanical relaxation of the fiber holders during repeated measurements as the current increased from 0 to 16 mA, (ii) random fluctuations due to noise, and (iii) variations of the Fabry-Perot (FP) oscillations resulting from reflections at the waveguide ends. This FP interference is shown in the broad spectral sum transmissions shown in Fig. 5(b) whose overall lineshape reflects the grating transmission. At longer wavelengths, the signal-to-noise

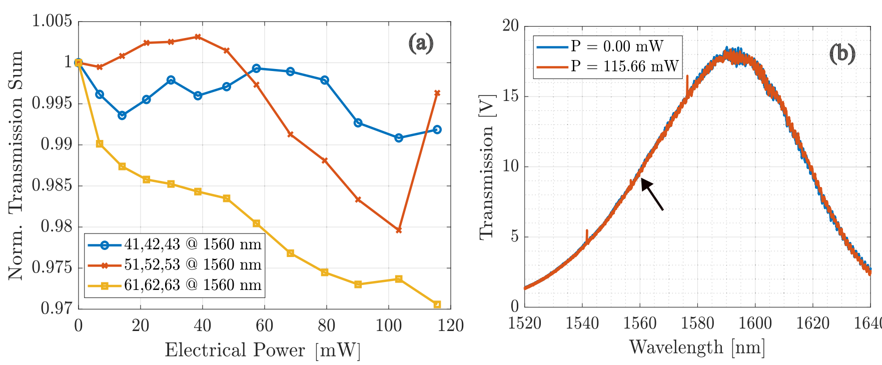

Fig. 5. (a) shows the sum of three outputs (41+42+43, 51+52+53, and 61+62+63) normalized to the zero applied electrical power as a function of the electrical power applied to the microheater for 1560 nm. (b) shows the 51+52+53 spectral transmission for two applied electrical powers: $P = 0\,\text{mW}$ and $P = 115.19\,\text{mW}$. The arrow refers to the wavelength used in (a).

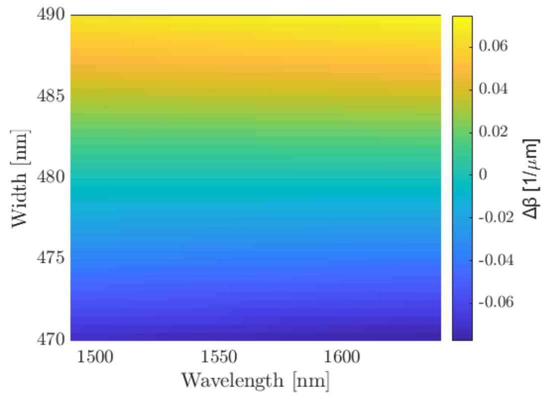

Fig. 6. Simulation results showing the variation of $\Delta\beta$ (the propagation constant difference) as a function of waveguide width and operating wavelength.

ratio is lower, and the FP fringes are more prominent compared to shorter wavelengths. The propagation losses are estimated to be approximately 2 dB cm^{-1} at 1550 nm, according to the foundry data. Given the short length of the 3×3 coupler waveguides (about 310 μm), the device losses are negligible. We also observed a grating insertion loss of less than 3 dB.

To further support our interpretation given in section 3.2 that a waveguide-width deviation of approximately 7 nm can explain the measured $\Delta\beta$, we performed numerical simulations using COMSOL Multiphysics. Figure 6 shows a color map of $\Delta\beta$ as a function of wavelength and waveguide width.

Funding. Provincia Autonoma di Trento (Q@TN); European Social Fund Plus (FSE-REACT-EU,PON 2014 - 2020).

Acknowledgments. We gratefully thank Dr. Iacopo Carusotto for useful suggestions and interesting discussions. S. Biasi acknowledges the co-financing of the European Union FSE-REACT-EU, PON Research and Innovation 2014–2020 DM1062/2021. S. Ali acknowledges the co-financing of PAT through the Q@TN joint lab.

Disclosures. The authors declare no conflicts of interest.

Author contributions. S.A., S.B. and R.F. performed the experiments. L.P., S.B., R.F., S.A. and B.A. conceived the study. S.A. performed the data analysis. All authors discussed the results and wrote the manuscript. All authors have read and agreed to the published version of the manuscript.

Data availability. Data supporting the findings of this study are available from the corresponding author upon a reasonable request.

References

1. C. E. Rüter, K. G. Makris, R. El-Ganainy, *et al.*, "Observation of parity–time symmetry in optics," Nat. Phys. **6**(3), 192–195 (2010).
2. H. Price, Y. Chong, A. Khanikaev, *et al.*, "Roadmap on topological photonics," J. Phys. Photonics **4**(3), 032501 (2022).
3. H. B. Perets, Y. Lahini, F. Pozzi, *et al.*, "Realization of quantum walks with negligible decoherence in waveguide lattices," Phys. Rev. Lett. **100**(17), 170506 (2008).
4. A. Peruzzo, M. Lobino, J. C. Matthews, *et al.*, "Quantum walks of correlated photons," Science **329**(5998), 1500–1503 (2010).
5. S. Biasi, G. Donati, A. Lugnan, *et al.*, "Photonic neural networks based on integrated silicon microresonators," Intell Comput **3**, 0067 (2024).
6. A. Lugnan, S. Aggarwal, F. Brückerhoff-Plückelmann, *et al.*, "Emergent self-adaptation in an integrated photonic neural network for backpropagation-free learning," Adv. Sci. **12**(2), 2404920 (2025).
7. L. B. Soldano and E. C. Pennings, "Optical multi-mode interference devices based on self-imaging: principles and applications," J. Lightwave Technol. **13**(4), 615–627 (1995).
8. H. Kogelnik and R. V. Schmidt, "Switched directional couplers with alternating $\delta\beta$," IEEE J. Quantum Electron. **12**(7), 396–401 (1976).
9. Y. Li, L. Zhang, M. Song, *et al.*, "Coupled-ring-resonator-based silicon modulator for enhanced performance," Opt. Express **16**(17), 13342–13348 (2008).

Optics EXPRESS

10. R. Menchon-Enrich, A. Llobera, V. J. Cadarso, *et al.*, "Adiabatic passage of light in cmos-compatible silicon oxide integrated rib waveguides," IEEE Photonics Technol. Lett. **24**(7), 536–538 (2012).
11. R. Menchon-Enrich, A. Llobera, J. Vila-Planas, *et al.*, "Light spectral filtering based on spatial adiabatic passage," Light:Sci. Appl. **2**(8), e90 (2013).
12. V. Evangelakos, E. Paspalakis, and D. Stefanatos, "Efficient light transfer in coupled nonlinear triple waveguides using shortcuts to adiabaticity," Sci. Rep. **13**(1), 1368 (2023).
13. C.-M. Kim and Y.-J. Im, "Switching operations of three-waveguide optical switches," IEEE J. Sel. Top. Quantum Electron. **6**(1), 170–174 (2000).
14. I. L. Garanovich, S. Longhi, A. A. Sukhorukov, *et al.*, "Light propagation and localization in modulated photonic lattices and waveguides," Phys. Rep. **518**(1-2), 1–79 (2012).
15. M. Stegmaier and W. H. Pernice, "Broadband directional coupling in aluminum nitride nanophotonic circuits," Opt. Express **21**(6), 7304–7315 (2013).
16. A. Syahriar, H. Adam, D. Astharini, *et al.*, "Analysis of three paralel waveguides using coupled mode theory and the method of lines," in *International Seminar on Application for Technology of Information and Communication* (IEEE, 2016), pp. 174–178.
17. G. Schmitt, W. Wenzel, and K. Dolde, "Integrated optical 3x3-coupler on linbo3: Comparison between theory and experiment," in *5th European Conference on Integrated Optics*, vol. 1141 (SPIE, 1989), pp. 67–73.
18. D. Pustakhod, X. Huang, E. van Vliet, *et al.*, "Characterization of 3x3 and 4x4 multimode interference couplers in inp generic photonic integration technology," in *20th Annual Symposium of the IEEE Photonics Benelux Chapter* (2015), pp. 35–38.
19. R. K. Gupta, S. Chandran, and B. K. Das, "Wavelength-independent directional couplers for integrated silicon photonics," J. Lightwave Technol. **35**(22), 4916–4923 (2017).
20. T.-T. Le, "Microring resonator based on 3x3 general multimode interference structures using silicon waveguides for highly sensitive sensing and optical communication applications," Int. J. Appl. Sci. Eng. **11**, 31–39 (2013).
21. R. Shankar, *Principles of Quantum Mechanics* (Springer Science & Business Media, 2012).
22. A. L. Jones, "Coupling of optical fibers and scattering in fibers," J. Opt. Soc. Am. **55**(3), 261–271 (1965).
23. D. Marcuse, "Coupled mode theory of round optical fibers," Bell Syst. Tech. J. **52**(6), 817–842 (1973).
24. A. Yariv, "Coupled-mode theory for guided-wave optics," IEEE J. Quantum Electron. **9**(9), 919–933 (1973).
25. C. Paiva-Sánchez, E. Burgos-Inostroza, O. Jiménez, *et al.*, "Quantum tomography via equidistant states," Phys. Rev. A: At., Mol., Opt. Phys. **82**(3), 032115 (2010).